Numerical investigation of wave-induced flexible vegetation dynamics in 3D using a coupling between DualSPHysics and the FEA module of Project Chrono

El Rahi, Joe; Martínez-Estévez, Iván; Tagliafierro, Bonaventura; Domínguez, José M.; Crespo, Alejandro J.C.; Stratigaki, Vasiliki; Suzuki, Tomohiro; Troch, Peter

DOI
10.1016/j.oceaneng.2023.115227

Publication date
2023

Document Version
Final published version

Published in
Ocean Engineering

Citation (APA)
El Rahi, J., Martínez-Estévez, I., Tagliafierro, B., Domínguez, J. M., Crespo, A. J. C., Stratigaki, V., Suzuki, T., & Troch, P. (2023). Numerical investigation of wave-induced flexible vegetation dynamics in 3D using a coupling between DualSPHysics and the FEA module of Project Chrono. *Ocean Engineering*, *285*, Article 115227. https://doi.org/10.1016/j.oceaneng.2023.115227

Ocean Engineering 285 (2023) 115227

Contents lists available at ScienceDirect

Ocean Engineering

journal homepage: www.elsevier.com/locate/oceaneng

Numerical investigation of wave-induced flexible vegetation dynamics in 3D using a coupling between DualSPHysics and the FEA module of Project Chrono

Joe El Rahi [a,*], Iván Martínez-Estévez [b], Bonaventura Tagliafierro [c], José M. Domínguez [b], Alejandro J.C. Crespo [b], Vasiliki Stratigaki [a], Tomohiro Suzuki [d,e], Peter Troch [a]

[a] Department of Civil Engineering, Ghent University, Technologiepark 60, 9052, Ghent, Belgium
[b] Environmental Physics Laboratory, CIM-UVIGO, Universidade de Vigo, Campus As Lagoas, 32004, Ourense, Spain
[c] Department of Civil and Environmental Engineering (DECA), Universitat Politecnica de Catalunya, Jordi Girona, 08034, Barcelona, Catalunya, Spain
[d] Flanders Hydraulics, Berchemlei 115, 2140, Antwerp, Belgium
[e] Department of Hydraulic Engineering, Delft University of Technology, Stevinweg 1, 2628CN, Delft, The Netherlands

ARTICLE INFO

Keywords:
Wave–vegetation interaction
Vegetation dynamics
Fluid–elastic structure interaction
SPH-FEA coupling
DualSPHysics
ProjectChrono

ABSTRACT

Vegetation meadows in coastal waters are a key constituent of a future green defense package due to the ecosystem services they provide and the potential to attenuate wave energy. To numerically describe the vegetation dynamics under wave action, this paper presents a novel application of a numerical coupling for solving fluid–elastic structure interactions (FSI) problems involving ultra-thin elements in a 3-D environment. The extended two-way coupling employed in this work combines the mesh-free Smoothed Particle Hydrodynamics (SPH) method in the DualSPHysics code to solve the fluid flow, and the Finite Element Analysis (FEA) structural solver in Project Chrono to solve the structural dynamics. To represent the vegetation, a flexible structure based on the Euler–Bernoulli beam model is used. The beam element is embedded into the SPH domain using an envelope subdomain that is discretized using dummy boundary particles. As such, this dummy envelope serves as a decoupling interface for the geometrical properties of the structure, allowing for ultra-thin structures smaller than the initial inter-particle distance (*dp*). The numerical approach is validated against an experimental setup including a flexible blade swaying under the action of an oscillatory flow. The results demonstrate that the numerical model is able to resolve the wave–vegetation interaction problem. Furthermore, additional insights into the blade dynamics reveal that the swaying velocity increases linearly along the length, with the upper part swaying at a speed comparable to the fluid velocity while the stem remains relatively stationary. Additionally, the findings indicate that rigid vegetation experiences higher forces per unit length, and in systems with substantial swaying motion, energy dissipation predominantly occurs around the lower base of the vegetation.

1. Introduction

Coastal hazards caused by increased storm frequency and intensity, along with accelerating sea level rise and urban development pose a threat to coastal communities and property worldwide (Glavovic et al., 2022). To counterbalance the increased risk, a diverse adaptation strategy consisting of conventional, hard infrastructure, combined with nature-based coastal defense systems, is able to offer a reliable and cost-effective solution (Narayan et al., 2016; Vuik et al., 2016). Coastal ecosystems such as seagrass meadows are an example of a green solution that can substitute (or complement) artificial structures for coastal defense systems (Ondiviela et al., 2014). Seagrasses naturally occur in shallow waters in the littoral zone where light is abundant (Ralph et al., 2007). They form meadows that can occupy large areas of seabed, exclusively in sandy or muddy sediments (Hemminga and Duarte, 2000). Seagrasses reduce erosion and limit sediment resuspension through the roots and rhizomes that grow beneath the sediment layer (Koch et al., 2006). In the water column, the vegetation stems interact with the oscillatory flow through a swaying motion (Luhar et al., 2010, 2013). This wave–vegetation interaction reduces the wave height through the generated drag that attenuates wave energy (Nepf, 1999). The reduction in wave heights has been documented in data collected from field measurements (e.g., *Zostera noltii* Paul and Amos, 2011, and

* Corresponding author.
E-mail address: joe.elrahi@ugent.be (J. El Rahi).

https://doi.org/10.1016/j.oceaneng.2023.115227
Received 27 March 2023; Received in revised form 9 June 2023; Accepted 22 June 2023
Available online 10 July 2023

Zostera marina Reidenbach and Thomas, 2018) and laboratory studies (e.g., experiments using mimic vegetation Stratigaki et al., 2011; Hu et al., 2014).

To scale up the utilization of vegetation meadows in future coastal defense systems, an explicit quantification of its effectiveness in suppressing wave energy under different flow conditions is required. Field measurements and physical experimental campaigns do offer insights into the characteristics of the flow. Nevertheless, on the downside, they require a lot of effort and resources. Numerical models, on the other hand, are a good alternative that can test a wide range of parameters within controlled environments and offer an in-depth view over the kinematics and dynamics. Numerical methods used in simulating wave–vegetation interaction can be classified into four main categories, characterized by: (i) using a porous medium (Hadadpour et al., 2019; Zinke, 2012); (ii) tuning the bed roughness factor (Chen et al., 2007; Augustin et al., 2009); (iii) using the drag force approach (Suzuki et al., 2019; Dalrymple et al., 1984); and (iv) modeling the flexibility using a structural solver (Paquier et al., 2021; Chen and Zou, 2019; Mattis et al., 2019; Yin et al., 2021; Zhu et al., 2020).

In the porous medium approach, the vegetation patch is modeled by fitting a porosity value equivalent to the proportion of pore space to total volume. The porosity value varies according to the vegetation patch characteristics and is determined through a fitting parameter. For instance, (i) (Hadadpour et al., 2019) calibrated the porosity value based on the leaf area index: a dimensionless parameter that accounts for vegetation length, leaf width and density; and (ii) (Zinke, 2012) used specific surface area and specific permeability terms. Another method is to model the energy dissipation through modifying the drag component in the bottom shear stress equations (Chen et al., 2007). There are several formulations used to calculate the modified drag coefficient term, such as the analytical solution presented in Kobayashi (1993) and further extended in Mendez et al. (1999) and Mendez and Losada (2004), and the modified drag coefficient equation presented in Nepf (1999) . All these formulations can successfully model the energy dissipation, but they remain limited in accuracy and applicability to a range of parameters such as flow features (e.g., Reynolds number) and vegetation characteristics.

A more explicit method involving the drag coefficient is the cylinder approach (Dalrymple et al., 1984) in which vegetation stems are represented using rigid cylinders. Subsequently, the energy dissipation is computed through the drag force expressed by the Morison equation (Morison et al., 1950). Suzuki et al. (2019) implemented this method into the non-hydro-static wave resolving code (SWASH, Zijlema et al., 2011), further extending it to account for inertial forces and porosity. The accuracy of this method remains sensitive to the drag coefficient (C_D) and the added mass coefficient (C_M) values that are determined either experimentally, or by using semi-empirical formulations (Keulegan and Carpenter, 1958; Sarpkaya and O'Keefe, 1996). Deriving the energy dissipation term in the fluid domain based on the assumption of rigid vegetation overestimates the wave attenuation by up to 70% (van Veelen et al., 2020).

Therefore, it is necessary to take flexibility into account by employing coupled fluid–structure interaction models. Kutija and Hong (1996) were among the first researchers to represent flexible vegetation using the cantilever beam theory. Several other papers have applied a similar principle to capture the vegetation flexibility by resolving the motion using structural solvers (Marjoribanks and Paul, 2022; Marjoribanks et al., 2014; Mattis et al., 2019; Brzenski and Davis, 2021; Mullarney and Henderson, 2010; Luhar and Nepf, 2016; Zeller et al., 2014; Paquier et al., 2021; Zhu et al., 2020; Yin et al., 2021). These models provide an accurate method to account for energy dissipation (e.g., simulating flexible vegetation with SWAN Yin et al., 2021), and they can also be applied to study the dynamics of a single blade under waves (e.g., Luhar and Nepf, 2016; Zhu et al., 2020) and combined wave–current systems (e.g., Zhu et al., 2020; Zeller et al., 2014).

To accurately capture the wave–vegetation interaction using numerical models, coupled fluid-structural solvers should avoid the use of any fitted parameters such as drag coefficient (C_D) and beam mechanical properties. This implies increased complexity, adaptive re-meshing tools, and numerically expensive simulations given the disparity between dimensions of the fluid domain and the very thin structural elements. The nature of the fluid–structure interaction problem in coastal environments involves violent flows and large structural deformations. It is in such conditions that Lagrangian solvers become advantageous over conventional mesh-based approaches. In fact, the Smoothed Particle Hydrodynamics (SPH) method (Monaghan, 1992) has been recently developed into well-established solvers for fluid–elastic structure interactions (FSI) dealing with violent flows impacting structures (e.g., flexible vegetation Paquier et al., 2021, hydro elastic slamming Khayyer et al., 2018). By definition, such models exclusively employ the SPH method to resolve the fluid flow, whereas the kinematics of the solid particles are solved by either using an SPH formulation or a mesh-based approach.

Unified framework models that employ the SPH method to solve the structural dynamics (O'Connor and Rogers, 2021; Khayyer et al., 2018, 2021) are easier to integrate into SPH codes and require no special treatment for the boundary interface (Khayyer et al., 2018). Partitioned models, which resort to separate solvers for the structural dynamics do have their advantages in terms of robustness and maturity (Fourey et al., 2017; Capasso et al., 2022; Yang et al., 2012). Additionally, they can be advantageous in terms of accuracy since they are configured using a structural resolution that is independent (larger or finer) from the SPH resolution. The first instance of successfully using a coupled SPH model to simulate the wave–vegetation interaction has been recently published in the work of Paquier et al. (2021). The coupled model uses a partitioned approach, which relies on the slender rod theory to reproduce the swaying motion of the vegetation while the fluid is resolved using the SPH method. This is achieved through applying a scaling law to accommodate the thin vegetation elements. Otherwise, these thin elements would be out of the computational range of the model due to difficulties with resolving the small thickness in the numerical discretization.

In view of the characteristics of the fluid–elastic structure interaction problems confronted in resolving vegetation dynamics, the objective of this work is to introduce a novel embedded method which is able to capture the transfer of forces and vegetation dynamics using the SPH method. The embedded approach presented utilizes the two-way coupling framework introduced in Martínez-Estévez et al. (2023b) and extends its applications to allow for the modeling of flexible elements in 3-D.The model aims to simulate ultra-thin beam elements with a thickness smaller than the initial inter-particle distance (dp) by introducing the beam into the fluid domain through a coupling interface known as the dummy envelope. The two-way coupling scheme is introduced into DualSPHysics, an open-source software based on the SPH method (Domínguez et al., 2022) and released under the GNU Lesser General Public License (LGPL). DualSPHysics supports numerical wave paddles and is able to generate a wide range of wave conditions (Altomare et al., 2017; Domínguez et al., 2019). Moreover, it has been successfully utilized as an engineering tool for modeling coastal processes such as wave impacts on coastal structures and overtopping (Altomare et al., 2020; Suzuki et al., 2022; Gruwez et al., 2020; Zhang et al., 2018). For resolving multiphysics problems, DualSPHysics is also coupled to Project Chrono library (Tasora et al., 2016) to accommodate complex mechanical systems and multi-body conditions (Martínez-Estévez et al., 2023a). In addition, a coupling between DualSPHysics and the multiphysics library to solve FSI was presented in Martínez-Estévez et al. (2023b).

This paper addresses the need for a numerical tool able to solve fluid–elastic structure interactions to investigate the vegetation dynamics and response to oscillatory flow. The numerical model is based on an

embedded approach which utilizes a dummy envelope to include ultra-thin structural elements into a large-scale fluid domain. The structural element is based on the Euler–Bernoulli beam and requires minimal computational effort regardless of the global SPH resolution (*dp*) used. In the following sections, the coupling is described with more details (Section 2) and then validated against 3-D experiments in Section 3. The blade dynamics and interpretation of the results are presented in Section 4, followed by limitations and future directions in Section 5, with conclusions to follow in the last section.

2. Methods

2.1. SPH formulation

In the SPH method, the governing equations are discretized in space using particles referring to data points where physical quantities such as velocity, pressure, position, and density are defined. The dynamics of the particles are computed based on the physical quantities of the neighboring particles. A distance function controls the list of neighboring particles. To solve the motion of the particles, the neighbor list is computed and the physical quantities are updated at each time step.

In fluid mechanics, the differential form of the Navier–Stokes (NS) equations can be rearranged into an equivalent form suitable for the SPH method using a continuous integral function, termed "kernel function, *W*". The kernel can be used to represent any function $f(\boldsymbol{r})$ in a domain Ω by:

$$f(\boldsymbol{r}) = \int f(\boldsymbol{r}')W(\boldsymbol{r}-\boldsymbol{r}', h)d\boldsymbol{r}' \tag{1}$$

For a set of particles, N, Eq. (1) can be solved for a particle a, with the summation including all neighboring particles, b, that fall within the influence radius defined by the smoothing length h (Eq. (2)):

$$f(\boldsymbol{r}_a) = \sum_j f(\boldsymbol{r}_b)\frac{m_b}{\rho_b}W(\boldsymbol{r}_b-\boldsymbol{r}_a, h) \tag{2}$$

where the physical quantities mass and density of the particles are denoted by m and ρ, respectively. In this study, the fifth order Wendland kernel (Wendland, 1995) given by Eq. (3) is used:

$$W(\boldsymbol{r}, h) = \alpha_D \begin{cases} \left(1-\frac{q}{2}\right)^4(2q+1) & 0 \le q \le 2, \\ 0 & 2 \le q \end{cases} \tag{3}$$

where q is equal to the ratio between the distance ($\mathbf{r}_{ab}$) separating the two particles a and b and the smoothing length h. The value of α_D is $7/4\pi$ in 2-D and $21/16\pi$ in 3-D.

The mass and momentum conservation equations for fluid mechanics in a continuum are expressed using the Lagrangian form of the Navier–Stokes equations in continuum, expressed as:

$$\frac{d\rho}{dt} = -\rho\nabla.\mathbf{v} \tag{4}$$

$$\frac{d\mathbf{v}}{dt} = -\frac{1}{\rho}\nabla P + \mathbf{g} + \boldsymbol{\Gamma} + D \tag{5}$$

where $\mathbf{v}$, $\mathbf{g}$, and P, are the velocity vector, gravity, and pressure, respectively; the dissipation terms are denoted by Γ, and the numerical density diffusion term by D. The Laminar viscosity (Lo and Shao, 2002) and Sub-Particle Scale (SPS) Turbulence (Gotoh et al., 2001; Dalrymple and Rogers, 2006) are the dissipative models utilized in this study. For brevity, these models are denoted as laminar + SPS in the following sections of the paper. The laminar viscosity term can be expressed as:

$$\nu_0\nabla^2\mathbf{v}_a = \sum_b m_b\left(\frac{4\nu_0 r_{ab}\cdot\nabla_a W_{ab}}{(\rho_b+\rho_a)(r_{ab}^2+\eta^2)}\right)\mathbf{v}_{ab} \tag{6}$$

where ν_0 is the kinematic viscosity of the fluid (10^{-6} m^2 s^{-1} for water) and the parameter $\eta = 0.001h^2$, used to avoid zero values when the distance ($\mathbf{r}_{ab}$) is very small. By defining the dissipative term in the momentum equation using Eq. (6) and adding the SPS stress tensor τ, Eq. (5) can be rewritten as:

$$\frac{d\mathbf{v}}{dt} = -\frac{1}{\rho}\nabla P + \mathbf{g} + \nu_0\nabla^2\mathbf{v}_a + \frac{1}{\rho}\nabla\tau \tag{7}$$

The work of Dalrymple and Rogers (2006) describes the implementation of the SPS stress tensor in DualSPHysics using Einstein notation over directions i and j:

$$\frac{\tau^{ij}}{\rho} = 2\upsilon_{SPS}(S^{ij} - \frac{1}{3}S^{ij}\delta^{ij}) - \frac{2}{3}C_I\Delta^2\delta ij\left|S^{ij}\right|^2 \tag{8}$$

where Δ is the initial inter-particle distance (*dp*), and C_I is set to 0.00066 (following Blin et al., 2003 and as mentioned in Dalrymple and Rogers, 2006). The eddy viscosity term is defined as $\nu_{SPS} = [C_s\Delta]^2\left|S^{ij}\right|^2$, with $C_s = 0.12$ being the Smagorinsky constant (Smagorinsky, 1963). The local strain rate $\left|S^{ij}\right| = 1/2(2S^{ij}S^{ij})^{1/2}$ with S^{ij} being the strain tensor computed using the i and j components of the velocity field. By replacing the laminar and SPS dissipation terms, the momentum equation (Eq. (9)) is expanded into:

$$\begin{aligned}\frac{d\mathbf{v}_a}{dt} &= \sum_b m_b\left(\frac{P_b+P_a}{\rho_b\rho_a}\right)\nabla_a W_{ab} + \boldsymbol{g} \\ &+ \sum_b m_b\left(\frac{4\nu_0 r_{ab}\cdot\nabla_a W_{ab}}{(\rho_b+\rho_a)(r_{ab}^2+\eta^2)}\right)\mathbf{v}_{ab} \\ &+ \sum_b m_b\left(\frac{\tau_{ij}^b}{\rho_b^2}+\frac{\tau_{ij}^a}{\rho_a^2}\right)\nabla_i W_{ab} + D\end{aligned} \tag{9}$$

DualSPHysics is implemented using the weakly compressible form of SPH (WCSPH) (Monaghan, 1994) for fluids. This formulation couples the density and pressure fields by using Tait's equation of state (Batchelor, 2000) to determine the fluid pressure, P; all while allowing for small fluctuations in the density field. The pressure equation is shown in Eq. (13):

$$P = \frac{c_s^2\rho_0}{\gamma}\left[\left(\frac{\rho}{\rho_0}\right)^\gamma - 1\right] \tag{10}$$

where ρ_0 is the reference fluid density (1000 kg m^{-3}), γ is the polytropic constant (default value of 7 is used), and c_s is the speed of sound. Abrupt non-physical fluctuations of the density field might arise due to this formulation. To counteract this, DualSPHysics includes an additional diffusion term in the continuity equation. The density diffusion term (D) acts as a low-pass filter for upper-bound noise with low amplitude (Fourtakas et al., 2019).

2.2. FEA solver

Project Chrono is a C++ library that supports multiphysics simulations and operates under a BSD-3 license. Its core module includes a Finite Element Analysis (FEA) structural solver that enables the simulation of flexible structures (Tasora et al., 2016). This solver enables the simulation of flexible structures and implements a non-linear FEA through a co-rotational (CR) approach, as described in Felippa and Haugen (2005). Using this method, the deformable elements in the simulation can undergo significant deformations and rotations. The library also employs corotated 3-D Euler–Bernoulli to solve the flexible elements, which draws on the formulation introduced in Rankin and Nour-Omid (1988).

To model 3-D beams in simulations, they are divided into segments attached through nodes. The number of segments is denoted by N_s, while the number of nodes is $N_s + 1$. Each segment is represented as a 3-D Euler–Bernoulli beam, while the beam nodes are finite elements with six degrees of freedom (DOF). However, it should be noted that this approach works best when the shear effects are not significant. Users can define various section material properties such as density (ρ_s), damping (C_s), Young's Modulus (E), and Poisson's ratio (ν_s) to model the structure according to their specific requirements. By varying

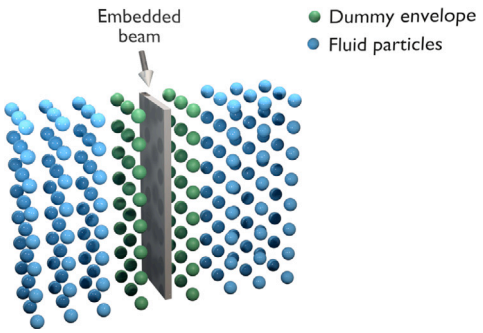

Fig. 1. Artist impression depicting the embedded beam inside the dummy envelope.

Table 1
Physical parameters of the numerical setup.

Hydrodynamic conditions	
Wave amplitude (a_w) [±0.10 cm]	3.90
Wave period [±0.10 s]	2.00
Water depth [m]	0.30
Wavelength [m]	3.25
Blade properties	
Length [m]	0.05, 0.10, 0.20
Thickness [±0.00004 m]	0.0004
Width [±0.0005 m]	0.02
Young's modulus [±0.08 GPa]	0.93
Density [±10 kg m^{-3}]	950
Poisson ratio [m s^{-1}]	0.46
Damping [C_s]	0.0075

these parameters, users can control the behavior of the beam elements in the simulation. For instance, adjusting the density will affect the mass of the beam and its response to external forces, while the Young's modulus determines its stiffness. The Poisson's ratio, on the other hand, affects the lateral deformation of the beam when it is subjected to axial loads. In summary, by defining these properties, users can create accurate simulations of 3-D beams using finite elements.

2.3. Coupling procedure

The numerical communication protocol between the two solvers is built over the novel implementation of the two-way coupling between DualSPHysics and the FEA module of Project Chrono presented in Martínez-Estévez et al. (2023b). In this study, the coupling is extended to provide support for 3-D simulations, thereby expanding the capabilities towards engineering applications. The flexible structure is introduced into the fluid domain through a dummy envelope discretized using boundary particles. While the height and width of the dummy envelope are identical to the dimensions of the embedded beam; the thickness is not restricted by any measurement, under the condition that a minimum value necessary for accurate fluid-force computations is used. A visual layout of the coupling is shown in Fig. 1. The pathway to solve the FSI in a single SPH time step (Δt_{SPH}) is shown in Fig. 2. First DualSPHysics computes the forces $\boldsymbol{F}$ exerted by the fluid on the structure. This is obtained by summing up the contribution of all neighboring fluid particles by applying Eqs. (11) and (12) (Domínguez et al., 2022):

$$\frac{dv}{dt}\Big|_{a\in K} = \sum_{b\in F} m_b \frac{dv_{ab}}{dt} \tag{11}$$

$$\mathbf{F} = \sum_{a\in K} m_a \frac{dv_a}{dt} \tag{12}$$

where $\boldsymbol{v}$ is the velocity, $a \in K$ refers to dummy boundary particles and $b \in F$ refers to the fluid particles.

The computed forces are communicated to Project Chrono and applied to the nodes. The structural deformations of the beam element are solved during a Δt_{SPH} by iterating multiple internal time steps (Δt_{CH}). Afterwards, Project Chrono transfers back the updated node positions (**R**) to DualSPHysics. The positions of the dummy particles are reshuffled accordingly to represent the deflected shape of the structure in the SPH domain. This pattern is repeated for every time step (Δt_{SPH}) until the maximum time of the simulation is reached. The work presented by Martínez-Estévez et al. (2023b) provides a detailed description of the coupling framework.

In the framework of this coupling, vegetation dynamics is addressed by resolving the balance between external excitation forces and internal resistance forces. In this case the external forces are made up of gravity, buoyancy, and the hydrodynamic forces applied by the waves. These are computed within the SPH environment using the standard SPH kernel. The internal resistance is calculated by assuming that the vegetation behaves like a cantilever beam of uniform stiffness (Euler–Bernoulli beam). As such the deflection along the beam is calculated using the following equation:

$$q(x) = -\phi(x)\left(EI\frac{d\phi(x)}{dx}\right) \tag{13}$$

where $q(x)$ and $\phi(x)$ represent the transverse load at position x and the displacement at position x respectively; E represents the Young's Modulus, and I represents the second moment of inertia of the cross-section. The product of E and I is referred to as the flexural rigidity. When solving the system, the mass, damping, and stiffness matrices are incorporated.

3. Results: numerical model validation

The numerical model is applied and validated using experimental results of a flexible blade swaying under the forcing of a wave-induced oscillatory flow. The experimental setup is described in Luhar and Nepf (2016) and consists of a flexible plastic polymer blade fixed on top of a trapezoidal measurement box situated in the center of a 24 m-long, 38 cm-wide, and 60-cm-deep wave flume fitted with a paddle wave maker. Regular waves are generated until a periodic blade motion is achieved, and the blade-tip excursions, horizontal water velocity, and horizontal force component are measured.

The wave conditions and blade geometric and mechanical properties are shown in Table 1. Three sets of experiments with identical wave conditions and different blade lengths: (i) l = 0.05 m, (ii) l = 0.10 m, and (iii) l = 0.20 m; are used for validation. To optimize the numerical runtime, the wave tank is scaled down, maintaining a distance of approximately one wavelength (L) between the paddle and the blade, and half a wavelength ($1/2\,L$) between the blade position and the absorption beach. In the y-direction, a clearance of two blade width (b) is maintained to minimize interference from the lateral boundaries. The schematic of the numerical wave flume is shown in Fig. 3.

3.1. Hydrodynamic conditions

Prior to comparing the transfer of forces and blade excursions, the numerical tank setup is tested without the flexible blade to ensure proper wave propagation and accurate velocity fields. The numerical wave tank is created using an inter particle spacing, being dp = 0.004 m. On one side of the tank, the wave paddle is placed at an adequate distance from the blade location to ensure proper wave propagation. On the other side, a numerical beach with velocity damping is created to absorb the incident waves and limit reflection. The lateral boundaries are configured using periodic conditions, with a total lateral clearance of 12 cm, equivalent to 6 plate widths. The setup adds up to 3.6 million particles and takes approximately 1.15 h to run a 1 s simulation on a GPU NVIDIA A100-SXM4 80 GB. To achieve a fully developed wave field and attain a periodic steady state, the simulation

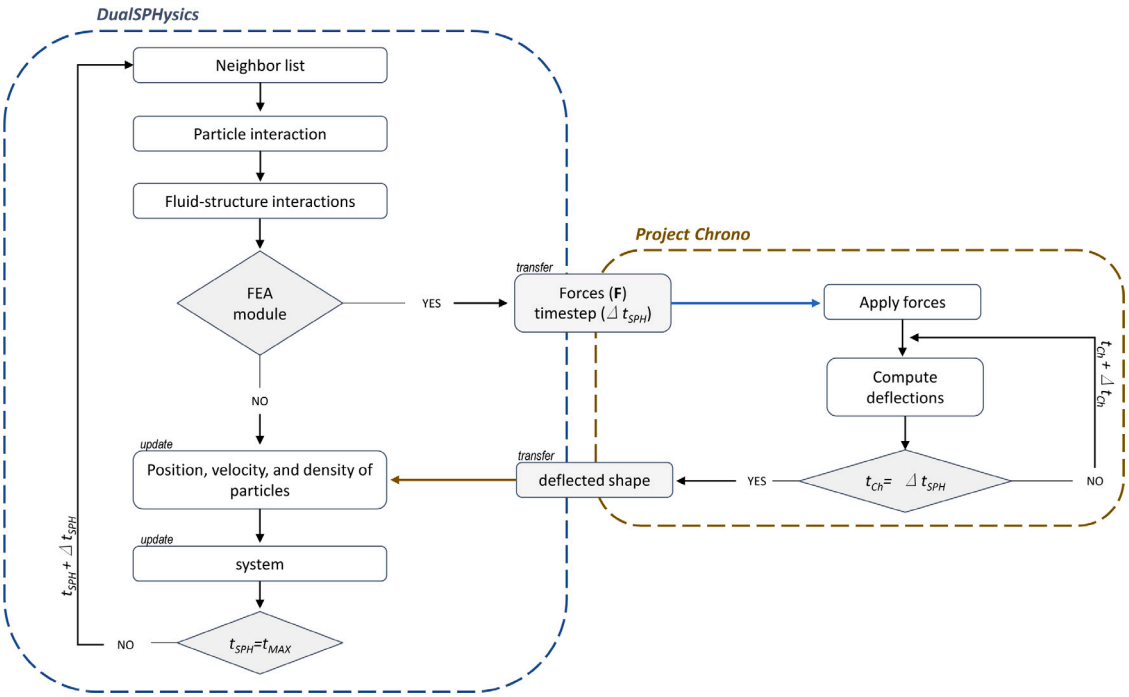

Fig. 2. Coupling scheme between DualSPHysics and Project Chrono.

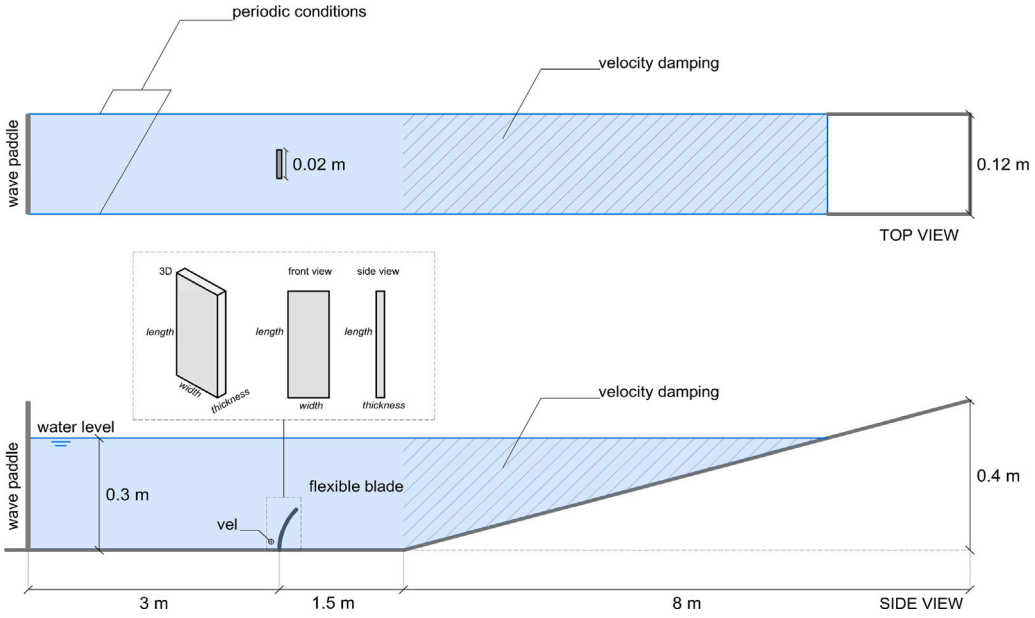

Fig. 3. Definition sketch of the numerical wave tank used to validate the experimental setup.

time is set to 25 s, allowing for an initial ramp-up period and 6 wave cycles.

Second order wave generation theory is used and the surface elevation is recorded using a numerical wave gauge placed at the location of the flexible blade. The horizontal velocity component is recorded 15 cm upstream of the flexible blade, starting from a minimum vertical position of 0.04 m (corresponds to the base of the blade). The locations chosen for measuring surface elevation and velocity follow the experimental setup, ensuring minimal interference between the blade and the measurements.

The measured surface elevations and horizontal wave velocities are shown in Fig. 4. The data acquired during the ramp-up period is plotted using light blue, while bold blue is used for the fully developed fields. To confirm that the paddle displacements are generating the target wave field, the plot also includes the theoretical surface elevation calculated using Stokes theory and displayed using a dashed navy blue line. The wave amplitude (a_w) is calculated for 6 wave cycles (bold blue line in upper plot) and equals to 3.99 cm with a reflection coefficient of 0.05; a perfect agreement with the experimental data (3.90 ± 0.10 cm). The horizontal velocity component, u_w, is plotted in the lower panel of Fig. 4, and has an average positive maximum magnitude of 0.202 m/s. This is in agreement with the maximum positive horizontal velocity measured in the experiments and equals to 0.206 m/s (displayed using the dotted black line in the lower panel of Fig. 4). For a detailed

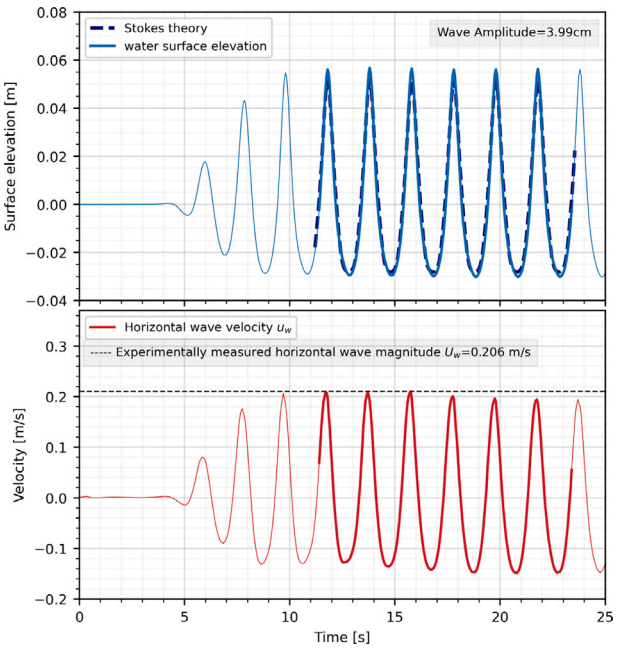

Fig. 4. Numerical results for the validation of the hydrodynamics (DualSPHysics): top panel shows the surface elevations, and lower panel shows the horizontal velocity component(u_w). The light color refers to data acquired during the ramp-up period, and the bold color refers to fully developed wave cycles. (*No blade in position*).

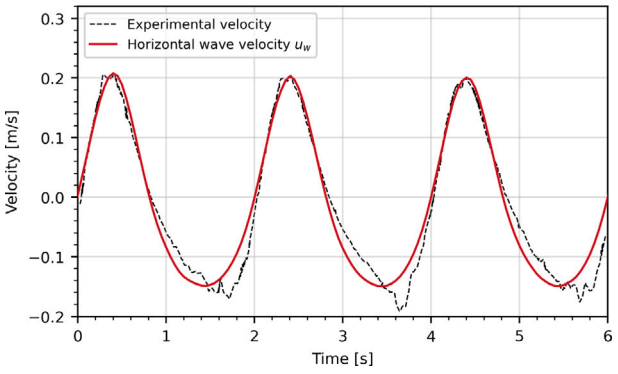

Fig. 5. Horizontal wave velocity component (u_w) computed using DualSPHysics plotted against experimental data obtained using PIV optical measurement technique (Luhar and Nepf, 2016). Measurements are plotted for a total duration of 6 s and refer to 3 cycles of fully developed waves. (*No blade in position*).

comparison of the horizontal velocity signal, the numerical results (red color) are plotted against the experimentally measured horizontal component (black dashed line) for 3 wave cycles in Fig. 5. As shown in the plot, the peaks and period of the numerically computed velocity match with the experimental measurements. The numerical model accurately reproduces a velocity signal with a dominant positive amplitude that is 60% larger than the minimum (negative) velocity. This lack of symmetry around the zero velocity axis (y = 0) is a characteristic of second order waves and expectedly creates velocity signals with large peaks and smaller troughs. Nonetheless, there is a small inconsistency in the shape of the troughs and in the minimum (negative) velocities. This disagreement is partly associated with the wave transformations present in the experimental flume. Altogether, the numerical results accurately reproduce the experimental flow conditions including the wave amplitude and period, and the velocity signal with acceptable deviations that have minimal affects on the fluid–structure interaction to be presented in the following sections.

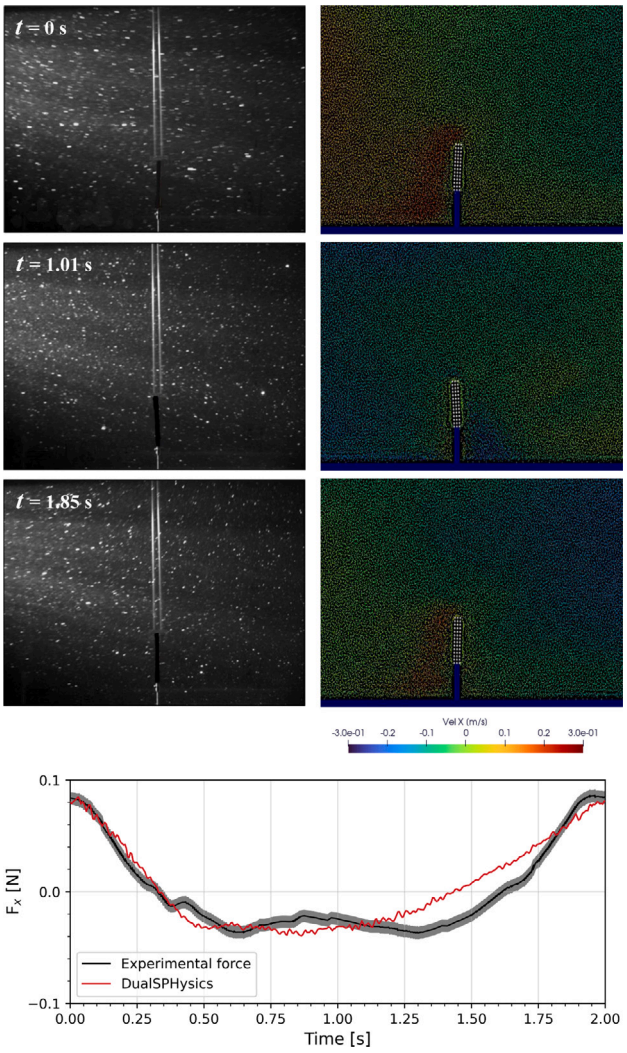

Fig. 6. Observed (left panels) (Luhar and Nepf, 2016) and simulated (right panels) beam (l = 5 cm) postures at different time instants, t. The experimentally and numerically computed horizontal force components (F_x) are shown in the lower panel. Visual comparison of blade posture is not to scale.

The numerical setup described in this section, including all parameters such as boundary conditions, inter-particle distance and wave generation settings, is used for validating the forces and dynamics of the flexible blade in the following sections.

3.2. Fluid–elastic structure interaction

3.2.1. Flexible blade with length l = 5 cm

The experimental setup using a flexible blade with length l = 5 cm is used as a first validation case to evaluate the proposed model. The numerical wave tank described in Section 3.1 (*Hydrodynamic conditions*) is used with the identical paddle displacements and inter-particle distance (dp = 0.004 m) of the first run to guarantee good agreement in terms of wave kinematics with the experiments. To model the flexible blade, an embedded Euler–Bernoulli beam element with a thickness of 0.000404 m is simulated using a dummy envelope which is identical in length and width, but with a thickness of 3 × dp (0.012 m). By using this configuration, the embedment ratio (R_{emb}) expressed as the ratio between the thickness of the dummy envelope (W_d) and the thickness of the embedded structural element (W_s) is equal to 29.7 (Eq. (14)).

$$R_{emb} = \frac{W_d}{W_s} \tag{14}$$

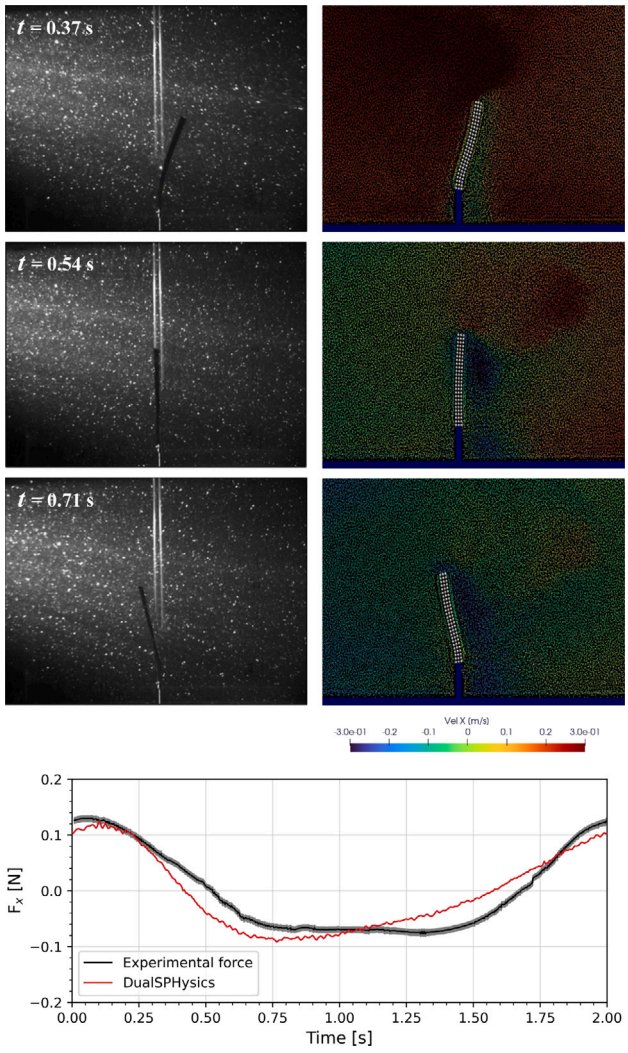

Fig. 7. Observed (left panels) (Luhar and Nepf, 2016) and simulated (right panels) beam (l = *10* cm) postures at different time instants, t. The experimentally and numerically computed horizontal force components (F_x) are shown in the lower panel. Visual comparison of blade posture is not to scale.

The nonconformity created by the difference in thickness leads to nonphysical lateral bending along the x-axis. Therefore, the laterally transferred forces along the y-axis between the fluid particles and the dummy particles are blocked. Regarding the structural solver, the beam element is constructed using five segments and configured using the physical and mechanical properties as reported in the experiments (Luhar and Nepf, 2016). Even though the authors in Luhar and Nepf (2016) remark a small degree of curvature in the neutral posture of the beam, which may lead to an increase in flexural rigidity, no corrections for the modulus of elasticity (E) or calibration of the damping ratio were performed. From a structural standpoint, the determination of the flexural rigidity of the beam directly influences both the maximum deflection and the period of oscillations. However, the present study did not explore the sensitivity of blade swaying to variations in the modulus of elasticity (E).

The numerical simulation is launched for a physical time of 25 s to accommodate the initial ramp-up period and achieve periodic steady state in terms of wave propagation, velocity fields, and fluid–structure interaction. Fig. 6 shows the blade posture (i) captured in the experiments in the left panels and (ii) simulated in the numerical model in the right panels. Each row corresponds to a different time instant (t), with the three rows overlaying most of the wave cycle starting from t = 0 s to t = 1.85 s. The blade, highlighted with bold black, maintains a vertical posture during the entire wave cycle in the experiments (left panels) and in the numerical model (right panels).

The lower panel of Fig. 6 shows the horizontal component of the forces (F_x) as recorded in the experiments (gray color) and as computed by DualSPHysics (red color). The 10% accuracy of the load cell used in the experiments is highlighted using a gray shade. To get a more representative value, the DualSPHysics forces shown are averaged over 6 wave cycles. Referring to the lower panel of Fig. 6, the numerical model accurately captures the maximum forces at t = 0 s and t = 2 s. Additionally, the initial decrease in the force as well as the minimum (negative) force are well reproduced. Nevertheless, the time instant of minimum (negative) force is not accurately captured. The experimental force signal has a double trough, while the numerical force is quasi symmetric around the minimum; strictly decreasing during the initial half (1/2) cycle and then strictly increasing afterwards.

The results of this first test case with a flexible blade (l = 5 cm) portray the capacity of the numerical approach in capturing the transfer of forces and properly modeling the flexural rigidity and blade response in an environment of low hydrodynamic forcing. As the forces exerted by the fluid are not large enough to initiate swaying, the blade maintained a neutral posture over the wave cycle. More importantly, the results confirm the validity of the embedment approach used. The contrast in dimensions between the dummy envelope in the numerical domain and the blade in the experiments (dummy envelope larger than the structure, R_{emb} = 29.7) did not affect the transfer of forces. This proves that the embedment approach is valid for solving thin-structural elements in fluid environments where the forces are dominant along the face of the structure normal to the incident wave direction.

3.2.2. *Flexible blade with length l = 10 cm*

Considering the capability of the numerical method presented in resolving the fluid–elastic structure problem in a low hydrodynamic forcing environment, the next case investigates a blade with a lower flexural rigidity, more susceptible to wave-induced dynamics. The case setup is identical to the numerical setup previously described but with a flexible blade with a length l = 10 cm discretized using 10 segments. The increase in length by a factor of two reduces the bending stiffness of the beam and subjects the beam to greater forces due to the increase in surface area. Combined, these two factors will induce blade deflections in the form of a swaying motion under the action of the regular waves. The dimensions, physical and mechanical properties of the beam, as reported in Luhar and Nepf (2016), are once again used to configure the Euler beam. Additionally, the same thickness of the dummy envelope and the embedment ratio (R_{emb} = 29.7) reported in the previous test case (flexible blade with length l = 5 cm) are used. The simulation is executed for a total physical duration of 25 s, and the results are obtained after achieving a periodic steady state for the hydrodynamics and fluid–structure interaction. Fig. 7 displays a visual comparison of the blade posture and shows the horizontal force component (F_x) as (i) reported in the experiments and (ii) calculated by the model. The numerical model tends to accurately capture the swaying motion of the experimental blade and the horizontal force component with slight variations. For a more detailed understanding, three instants of the simulation and the forces obtained from the fluid are further discussed in what follows. The top left panel of Fig. 7 corresponds to instant t = 0.37 s (for a wave cycle of T = 2.00 s); during this instant the plot of the exerted forces has a negative slope, and the beam is experiencing a decrease in force following the maximum at instant t = 0 s. The second time instant, t = 0.54 s, shows the beam posture at a neutral position with comparably identical postures between the experimental and numerical model. Last, at t = 0.71 s, the beam excursion is similar for the experimental and numerical outputs, but a slight deviation in posture is evident. The deviation in the visual comparison is backed up by the forces shown in the lower panel. Once again, the numerical output is plotted with red and the experimental forces are shown in

gray, with a 10% margin of error highlighted using a light gray shading. The magnitude of the maximum and minimum (negative) forces are properly captured but not synchronized. The numerical model reproduces the decreasing slope of the force from instant $t = 0$ s till $t = 0.75$ s, to increase afterwards with a constant slope (compared to a variable slope in the experimental) until reaching the maximum force. In comparison, the experimental force (light gray) reaches a bottom plateau from time instant $t = 0.75$ s till $t = 1.35$ s.

Overall, the results demonstrate the ability of the numerical model to capture the swaying motion of the flexible blade. With the hydrodynamic forcing exceeding the structural bending resistance of the structure, the flexible blade sways under the action of waves. The exhibited swaying motion is verified by the experimental results visually and supported by the plots of the horizontally transferred forces. Following this verification of the numerical method, the next section investigates the blade dynamics and looks into the tip excursions for longer blades undergoing large deflections.

3.2.3. Flexible blade with length $l = 20$ cm

The hydrodynamic results, the transfer of forces, and blade deflections shown in the previous section demonstrate that the employed numerical coupling is able to resolve the fluid–elastic structure problem using the embedded beam approach. To further investigate the performance of the numerical model, a third test case with a flexible blade with length $l = 20$ cm is presented. With this configuration, the flexural rigidity of the blade is minimal and insufficient to guarantee structural stability in a dry environment. This implies that the fluid forces exerted on the blade are necessary for structural stability, and the hydrodynamic forcing will induce large deformations in the blade.

In what follows, the numerical results of the blade posture and the transferred forces are compared to the experimental results. In addition to that, the blade configuration over one wave cycle is presented alongside the velocity and range of the swaying motion. The numerical setup is identical to the configuration described in Section 3.2.1 (*Flexible blade with length $l = 5$ cm*) consisting of a numerical wave tank with a flexible blade placed at approximately 1 wavelength (L) from the wave paddle. The flexible blade is configured using the Euler–Bernoulli beam configuration with 20 segments and with a thickness of 0.000404 m embedded into an envelope with a thickness of 0.012 m; resulting in an embedment ratio (R_{emb}) equals to 29.7. Regular waves with an amplitude (a_w) equals to 3.9 cm and a period (T) of 2 s are generated for a duration of 25 s; and the transferred forces, blade swaying motion, and velocities are recorded.

The evolution of the blade posture over the wave cycle is presented in Fig. 8. The left panels show the images captured during the experiments, while the right panels display the numerical blade posture visualized using particles. At the first-time instant $t = 0$ s, shown in the first row, the blade in the numerical model stands at an upright position with a slight deformation into the direction of the wave action. Similarly, the blade posture captured in the experiments reveals a vertical posture but with a larger misalignment with the neutral vertical axis. For the second time instant, $t = 0.67$ s, the experimental and numerical blades sway in the same direction and show a similar deformed shape, but with the experimental blade undergoing a larger deformation. Last, at $t = 1.68$ s, the numerical model accurately reproduces the recoil of the blade into a backward leaning posture. The performance of the numerical model is further supported by the agreement shown in the computed horizontal force component (F_x). Referring to the forces plotted in the graph shown in Fig. 8, the numerical model accurately captures the instant and magnitude of maximum force. Following the maximum force at $t = 0$ s, the numerical model accurately reproduces the decrease in force for the first 0.5 s, to later maintain the same negative slope until reaching the minimum (negative) force at $t = 1$ s. The magnitude of the minimum (negative) force is properly captured but is out of phase. The experimentally recorded force flattens out after the first 0.5 s to further drop afterwards reaching the minimum

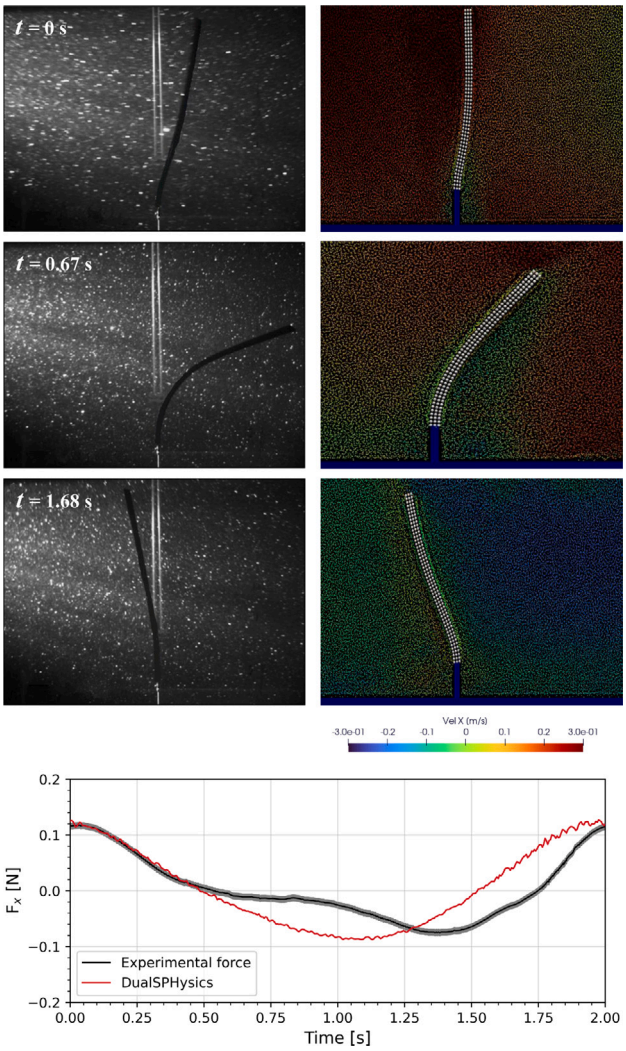

Fig. 8. Observed (left panels) (Luhar and Nepf, 2016) and simulated (right panels) beam ($l = 20$ cm) postures at different time instants, t. The experimentally and numerically computed horizontal force components (F_x) are shown in the lower panel. Visual comparison of blade posture is not to scale.

Table 2
Numerical model performance in terms of horizontal force component (F_x) across the three validation cases. Metrics presented are: RMSE, root mean square error;and MAE, mean absolute error.

Case	RMSE	MAE
l=5 cm	0.006	−0.002
l=10 cm	0.006	−0.002
l=20 cm	0.020	−0.002

(negative) force at $t = 1.35$ s. For the second half of the wave cycle, the numerical force increases at a comparatively similar slope to the experimental force and reaches the maximum force once again at $t = 2$ s. Overall, the numerical model properly characterizes the flexible blade swaying motion and accurately captures the magnitude of the horizontal force component. Yet, the constant decreasing trend of the numerical force component remains inconsistent with the experimental data. This may be attributed to the discrepancy in the trough velocity signal shown in Fig. 5 (Section 3.1. Hydrodynamic conditions) and to the effect of the curvature in the neutral posture of the beam.

To quantify the model's performance across the three presented validation cases, a tabulated representation of the errors is presented in Table 2. This information serves as a valuable tool for comprehending

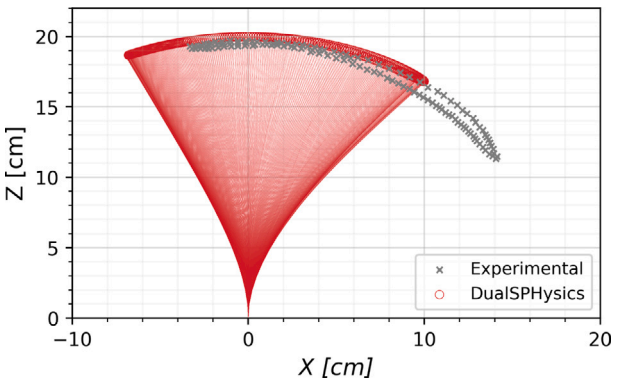

Fig. 9. Comparison of the horizontal (X) and vertical (Z) tip excursions of the blade over a wave period between the numerical coupling and experiments.

the model's effectiveness concerning the transferred forces (F_x), which exert a direct influence on the resolved blade dynamics. Furthermore, it promotes transparency and enables other studies to compare their metrics with those of the model presented here. For the three validation cases with increasing blade length (l = 5, 10, and 20 cm) the root mean square error (RMSE), and the mean absolute error (MAE) are shown. The RMSE reveals a good model performance with 0.006 N for the l = 5 cm and l = 10 cm blades. The error increases to 0.020 N for the l = 20 cm blade. In the second column of the table, the negative MAE values show that the model is systematically overpredicting the computed horizontal force component (F_x) across all three cases. The consistently negative MAE values observed align with the expectation derived from the previously presented results, wherein the numerically computed force consistently exceeded the experimental force during the second half of the wave cycle (refer to the lower panels of Figs. 6, 7, and 8). Lastly, the RMSE indicates that the model more accurately captures the dynamics of the shorter blades, which exhibit a smaller range of swaying.

An additional marker for the performance of the numerical model is the range of swaying at the crown of the blade, or the extreme tip. The range of swaying is defined as the largest horizontal distance between the points of extreme deflection at the crown of the blade. The swaying motion described by the numerical model is shown in Fig. 9. The position of the crown over one wave period is plotted using the red circles and the blade posture is depicted with the light red lines. For comparison, the location of the crown in the experiments is marked using the light gray cross hairs "x". The flexible blade in the numerical model shows a forward leaning dominated cycle, with the maximum deflection in the forward (positive) direction being 10.2 cm, around 43% larger than the backward (negative) deflection that stands at 7.1 cm. This tendency to deflect more in the positive direction is supported by the experimental data and can be attributed to the nature of the hydrodynamic forcing generated by the waves. As previously shown in Section 3.1 (Hydrodynamic conditions), the second order waves generated create a velocity field that is not symmetric around the zero-velocity axis and characterized by a larger positive velocity. While the numerical model underestimates the forward swaying motion and overestimates the recoil of the blade, the range of swaying is accurate at 17.4 cm compared to an experimental value of approximately 17.5 cm. The similarity in the range of swaying along with the plots of the transferred forces (F_x), refer to Fig. 8, indicate that there is a shift between the numerical and experimental blades. Probably this again can be attributed to the definition of the blade properties, and the inadequacy of the structural parameters to properly describe the effect of the curvature in the neutral posture of the blade.

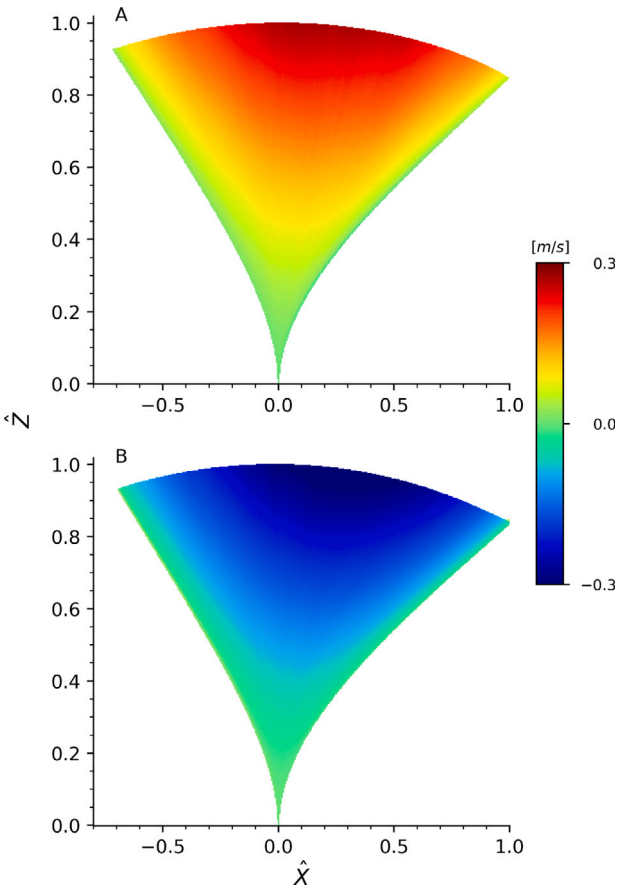

Fig. 10. Blade velocities during the two cycles: (A) shows the forward swing and (B) shows the recoil swing. The x-axis and y-axis make reference to the normalized deflection ($\hat{X}$) and the normalized blade length ($\hat{Z}$) respectively. A jet colormap is used for the horizontal blade velocity.

4. Blade dynamics

To project the results of the numerical model on the wave-vegetation interaction problem it is important to look into the blade dynamics. The oscillation velocity and the induced forces are directly linked, and interchangeably influence one another. Notice how an increase in the surface area by a factor of 4 between the 5 cm and 20 cm flexible blades only brought up a increase of 0.03 N; from a maximum horizontal force of 0.08 N (l = 5 cm) to 0.11 N (l = 20 cm). Also recall how the largest flexible blade with l = 20 cm experienced a similar minimum (negative) force, equals to −0.09 N, just like the 10 cm flexible blade. As for the maximum positive force, the difference between these two blades was only 0.01 N. Altogether, this demonstrates that a large range of swaying suppresses the increase in force. This is further verified by the oscillation velocity over the wave cycle shown in Fig. 10.

The swaying motion of the blade during a single cycle is divided into two distinct phases: (i) the forward swing shown in the top plot (plot A, Fig. 10), and (ii) the recoil swing shown in the bottom plot (plot B, Fig. 10). The forward swing describes the forward motion of the blade from the minimum to the maximum horizontal location, being "$\hat{X} = 1$" where "$\hat{X}$" is the normalized deflection calculated by dividing the deflection at any point by the maximum deflection measured. In contrast, the recoil swing describes the opposite cycle going from the maximum to the minimum horizontal location. For both cycles shown in Fig. 10, the vertical position of the blade is non-dimensionalized by dividing it by the blade length, l, shown as $\hat{Z}$. Furthermore, to differentiate between the two cycles, the horizontal blade velocity is

visualized through the utilization of a color palette. By examining the distribution of colors, it becomes possible to distinguish between the cycles, as each cycle is characterized by either exclusively positive or exclusively negative velocities.

Three main characteristics of the swaying motion can be identified from the two plots; first, in the region from $\hat{Z} = 0$ to $\hat{Z} = 0.3$, which corresponds to the base of the blade, there is a consistent maintenance of negligible blade velocity in close proximity to zero throughout the entire cycle. This negligible velocity is accompanied by a steady upright position of the blade up to $\hat{Z} = 0.05$, with a slight increase in the range of motion observed thereafter. Second, the increase in blade velocity starts at $\hat{Z} = 0.3$ and intensifies at $\hat{Z} = 0.7$. Within this zone, the blade's horizontal velocity ranges from approximately $\pm$ 0.2 to 0.3 m/s, which is comparable to the horizontal fluid velocity induced by the oscillatory flow. Notably, the absolute peak occurs at $\hat{X} = 0$ for both cycles. Third, during the forward and recoil swings, a retention zone bounds the area of high velocity at both ends. Within this transitional zone, where the velocity vector undergoes a change in orientation (from positive to negative and vice versa), the blade remains stationary for a brief period.

The magnitude of the transferred forces is determined by the disparity between the blade and fluid velocity. The characteristics of the swaying motion described earlier suggest that a significant force transfer occurs primarily in the lower base of the blade. As the upper sections of the blade swing at higher velocities, there is a diminishing gradient between the blade and fluid velocity. Consequently, the force transfer becomes less pronounced with these increased swinging velocities. These findings suggest that the hydrodynamic drag primarily originates from the base of the blade. This justifies the weak correlation between the blade's surface area and force transfer presented earlier in this section. Since the increase in surface area leads to higher swaying velocities, resulting in a reduced magnitude of force transfer along the passively swaying section of the blade.

5. Limitations and future directions

In this section, we examine the limitations that have emerged during the course of our investigation and directions for future advancements. First, the effectiveness of the presented numerical coupling has been validated for a single case where the numerical resolution used here provides acceptable results at a reasonable computational runtime. However, the applicability of the numerical tool to other wave conditions or stem dimensions needs to be extended in the future.

Second, one of the grand challenges in the SPH field is the lack of support for variable resolution (Grand Challenge 3 in Vacondio et al., 2021).The resolution of the simulations continues to pose limitations on the execution of the code. In the present research, to ensure the minimum possible thickness of the dummy envelope and a reasonable computational time, we make a compromise by discretizing the blade using 3 particles. This effectively prevents cross-boundary fluid interactions between fluid particles at both blade ends; however, it is important to note that the same boundary particles are neighboring fluid volumes from both ends at the same time. Despite the satisfactory results, it might be important to investigate this in future studies.

Third, conducting a convergence study is valuable for future research that explores flexible vegetation in SPH and seeks to expand upon the numerical coupling. The convergence and sensitivity analysis could address aspects such as SPH resolution to investigate the effects of using finer resolution on both the hydrodynamics and fluid–structure interaction. Additionally, the embedment ratio (R_{emb}) proposed in this work was selected to ensure the smallest possible thickness of the dummy envelope. However, with improved computational resources, it becomes important to explore smaller embedment ratios and establish guidelines for selecting appropriate values.

Last, the present study employs a two-way coupling with a highly efficient structural solver that resolves the swaying motion at a very low computational cost. This is supported by the findings presented in Martínez-Estévez et al. (2023b) and Capasso et al. (2022). Both studies demonstrate convergence in the solution when compared to benchmark cases with a limited number of segments. By extrapolating this approach to vegetation patches, the clear advantage of employing such a structural solver becomes evident.

6. Conclusion

Setting up a diversified portfolio for coastal defense systems that relies not only on hard coastal structures but also includes nature-based solutions such as vegetation meadows, is essential for mitigating future coastal hazards without disturbing the local ecosystems (Glavovic et al., 2022). From an engineering perspective, multiple challenges remain in the quantification of wave energy dissipation and the proper description of the vegetation dynamics.

In this paper, a novel numerical method for addressing the wave–vegetation interaction problem on the scale of the single vegetation blade was presented. The numerical method described in this paper relies on a partitioned approach where the flow and structural equations are solved separately. DualSPHysics, the fluid SPH solver, is coupled with an external structural library, Project Chrono, to include flexible Euler–Bernoulli beam elements. This approach benefits from the inherent strengths of the mesh-free codes in handling fluid dynamics and efficiency of mesh-based codes in solving structural deformations. This approach is able to handle ultra-thin structural elements with thicknesses smaller than the initial inter-particle distance (dp). This feature is realized through introducing a dummy envelope which serves as a decoupling interface for the geometric properties of the beam.

Experiments from Luhar and Nepf (2016) involving a thin flexible blade have been used as a reference for validation. The numerical model captured, with good agreement, the transfer of forces and deflections of the thin blade with a thickness ten times smaller than the fluid resolution (inter-particle distance, dp). More importantly, through comparing the blade velocities and range of swaying computed by the numerical model over multiple blades with increasing lengths; the model output characterized the wave attenuation potential of vegetation.

By projecting the results of the flexible blade on vegetation, the following conclusions can be made. First, the structural solver replicates the swaying motion of vegetation while effectively capturing the transfer of forces and the range of swaying. Second, the swaying velocity increases linearly along the length, reaching a maximum at the tip of the vegetation. While the upper part of the vegetation sways passively at a speed comparable to the fluid velocity, the stem is quasi-stationary and exhibits little swaying at negligible velocities. These characteristics of the swaying motion suggest that the hydrodynamic drag is primarily generated around the base of the vegetation. Third, the numerical simulations, which validate the experimental results, reinforce the notion that stiff vegetation experiences a greater horizontal force per unit length. That in turn (i) indicates a larger energy dissipation due to drag, and (ii) could potentially lead to a more pronounced wave height attenuation when extrapolated to cases with larger patches of vegetation. This latter point would need further investigation to confirm.

In the numerical model presented, no tuning or fitting parameters were employed neither in the fluid nor in the structural solvers. The results expose the sensitivity of the numerical coupling on the proper characterization of the structural parameters. While the bending stiffness and the forces are properly reproduced numerically, the oscillations tend to become non-synchronized with large deflections. As an improvement for future applications, defining the flexural stiffness based on dry tests could drastically improve the results.

Finally, this work will extend the range of applications of the mesh-free SPH method, allowing to include ultra-thin flexible structures in large domains. It offers a robust and efficient engineering

tool, which can simulate flexible vegetation dynamics in 3-D environments. It establishes the potential of the SPH method in addressing the wave–vegetation interaction problem and creates a framework, through the embedded approach, to maintain an acceptable computational cost. While the blade dynamics in this study were limited to oscillatory flows in intermediate water depths, future applications should benefit from the capability of the mesh-free method in handling violent flows and large deformations to look into the blade dynamics in the post-breaking inter-tidal areas. Future developments in code optimization, such as utilizing parallel processing with multiple GPUs and incorporating variable resolution techniques, hold the potential to significantly improve runtime efficiency for modeling large vegetation patches. Furthermore, these advancements could enable more accurate representation of complex interactions within the vegetation ecosystem.

CRediT authorship contribution statement

Joe El Rahi: Conceptualization of this study, Methodology, Validation, Formal analysis, Data Curation, Visualization, Writing – original draft, Editing. **Iván Martínez-Estévez:** Software, Methodology, Conceptualization of this study, Writing – review. **Bonaventura Tagliafierro:** Methodology, Conceptualization of this study, Writing – review. **José M. Domínguez:** Software, Supervision, Writing – review. **Alejandro J.C. Crespo:** Conceptualization, Supervision, Writing – review. **Vasiliki Stratigaki:** Supervision, Funding aquisition, Writing – review. **Tomohiro Suzuki:** Conceptualization, Supervision, Writing – review. **Peter Troch:** Conceptualization of this study, Methodology, Supervision, Project administration, Funding acquisition, Writing - Review and Editing.

Declaration of competing interest

The authors declare that they have no known competing financial interests or personal relationships that could have appeared to influence the work reported in this paper.

Data availability

No data was used for the research described in the article.

Acknowledgments

J. El Rahi is a Ph.D. fellow (fellowship 11l5821N) of the Research Foundation Flanders (FWO).

I. Martínez-Estévez acknowledges funding from Xunta de Galicia, Spain under “Programa de axudas á etapa predoutoral da Consellería de Cultura, Educación e Universidades da Xunta de Galicia” (ED481A-2021/337).

B. Tagliafierro gratefully acknowledges financial support for this publication by the Fulbright Schuman Program, which is administered by the Fulbright Commission in Brussels and jointly financed by the U.S. Department of State, United States, and the Directorate-General for Education, Youth, Sport and Culture (DG.EAC) of the European Commission. Its contents are solely the responsibility of the author and do not necessarily represent the official views of the Fulbright Program, the Government of the United States, or the Fulbright Commission in Brussels.

The computational resources used in this work were provided by the VSC (Vlaams Supercomputer Centrum), funded by the Research Foundation Flanders (FWO), Belgium and the Flemish Government, Belgium. In an effort to maintain an environment-friendly attitude, J. El Rahi acknowledges that he exclusively used green modes of transportation to commute during the period of this research.

References

Altomare, C., Domínguez, J., Crespo, A., González-Cao, J., Suzuki, T., Gómez-Gesteira, M., Troch, P., 2017. Long-crested wave generation and absorption for SPH-based DualSPHysics model. Coast. Eng. 127, 37–54. http://dx.doi.org/10.1016/j.coastaleng.2017.06.004, URL: https://www.sciencedirect.com/science/article/pii/S0378383916301831.

Altomare, C., Tafuni, A., Domínguez, J.M., Crespo, A.J., Gironella, X., Sospedra, J., 2020. SPH simulations of real sea waves impacting a large-scale structure. J. Mar. Sci. Eng. 8, 1–21. http://dx.doi.org/10.3390/jmse8100826.

Augustin, L.N., Irish, J.L., Lynett, P., 2009. Laboratory and numerical studies of wave damping by emergent and near-emergent wetland vegetation. Coast. Eng. 56 (3), 332–340. http://dx.doi.org/10.1016/j.coastaleng.2008.09.004, URL: https://www.sciencedirect.com/science/article/pii/S037838390800152X.

Batchelor, G.K., 2000. An Introduction to Fluid Dynamics. In: Cambridge Mathematical Library, Cambridge University Press, http://dx.doi.org/10.1017/CBO9780511800955.

Blin, L., Hadjadj, A., Vervisch, L., 2003. Large eddy simulation of turbulent flows in reversing systems. J. Turbul. 4 (1), 1. http://dx.doi.org/10.1088/1468-5248/4/1/001.

Brzenski, J., Davis, K., 2021. Flexible vegetation and its implementation in the swash ocean model. In: OCEANS 2021: San Diego – Porto. pp. 1–6. http://dx.doi.org/10.23919/OCEANS44145.2021.9705777.

Capasso, S., Tagliafierro, B., Martínez-Estévez, I., Domínguez, J.M., Crespo, A.J., Viccione, G., 2022. A DEM approach for simulating flexible beam elements with the project chrono core module in DualSPHysics. Comput. Part. Mech. http://dx.doi.org/10.1007/s40571-021-00451-9.

Chen, S.N., Sanford, L.P., Koch, E.W., Shi, F., North, E.W., 2007. A nearshore model to investigate the effects of seagrass bed geometry on wave attenuation and suspended sediment transport. Estuar. Coasts 30, 296–310. http://dx.doi.org/10.1007/BF02700172.

Chen, H., Zou, Q.P., 2019. Eulerian–Lagrangian flow-vegetation interaction model using immersed boundary method and OpenFOAM. Adv. Water Resour. 126, 176–192. http://dx.doi.org/10.1016/j.advwatres.2019.02.006.

Dalrymple, R.A., Hwang, P., Kirby, J.T., 1984. Wave diffraction due to areas of energy dissipation. J. Waterw. Port Coast. Ocean Eng. 1, 2–3. http://dx.doi.org/10.1061/(ASCE)0733-950X(1984)110.

Dalrymple, R., Rogers, B., 2006. Numerical modeling of water waves with the SPH method. Coast. Eng. 53 (2), 141–147. http://dx.doi.org/10.1016/j.coastaleng.2005.10.004, URL: https://www.sciencedirect.com/science/article/pii/S0378383905001304. Coastal Hydrodynamics and Morphodynamics.

Domínguez, J.M., Altomare, C., Gonzalez-Cao, J., Lomonaco, P., 2019. Towards a more complete tool for coastal engineering: Solitary wave generation, propagation and breaking in an SPH-based model. Coast. Eng. J. 61, 15–40. http://dx.doi.org/10.1080/21664250.2018.1560682.

Domínguez, J.M., Fourtakas, G., Altomare, C., Canelas, R.B., Tafuni, A., García-Feal, O., Martínez-Estévez, I., Mokos, A., Vacondio, R., Crespo, A.J.C., Rogers, B.D., Stansby, P.K., Gómez-Gesteira, M., 2022. DualSPHysics: from fluid dynamics to multiphysics problems. Comput. Part. Mech. 9, 867–895. http://dx.doi.org/10.1007/s40571-021-00404-2.

Felippa, C.A., Haugen, B., 2005. A unified formulation of small-strain corotational Finite elements: I. Theory. Comput. Methods Appl. Mech. Engrg. 194, 2285–2335. http://dx.doi.org/10.1016/j.cma.2004.07.035.

Fourey, G., Hermange, C., Le Touzé, D., Oger, G., 2017. An efficient FSI coupling strategy between Smoothed Particle Hydrodynamics and Finite Element Methods. Comput. Phys. Comm. 217, 66–81. http://dx.doi.org/10.1016/j.cpc.2017.04.005.

Fourtakas, G., Dominguez, J.M., Vacondio, R., Rogers, B.D., 2019. Local uniform stencil (LUST) boundary condition for arbitrary 3-D boundaries in parallel Smoothed Particle Hydrodynamics (SPH) models. Comput. & Fluids 190, 346–361. http://dx.doi.org/10.1016/j.compfluid.2019.06.009.

Glavovic, B., Dawson, R., Chow, W., Garschagen, M., Haasnoot, M., Singh, C., 2022. Cross-chapter 2: Cities and settlements by the sea. In: Pörtner, H.-O., Roberts, D.C., Tignor, M., Poloczanska, E.S., Mintenbeck, K., Alegría, A., Craig, M., Langsdorf, S., Löschke, S., Möller, V., Okem, A., Rama, B. (Eds.), Climate Change 2022: Impacts, Adaptation, and Vulnerability. Contribution of Working Group II to the Sixth Assessment Report of the Intergovernmental Panel on Climate Change. Cambridge University Press.

Gotoh, H., Shibahara, T., Sakai, T., Koshizuka, S., Yabe, T., 2001. Sub-particle-scale turbulence model for the MPS method - Lagrangian flow model for hydraulic engineering. Adv. Methods Comput. Fluid Dyn. Comput. Fluid Dyn. J. 9, 339–347, URL: https://www.tib.eu/de/suchen/id/BLSE%3ARN093974748.

Gruwez, V., Altomare, C., Suzuki, T., Streicher, M., Cappietti, L., Kortenhaus, A., Troch, P., 2020. An inter-model comparison for wave interactions with sea dikes on shallow foreshores. J. Mar. Sci. Eng. 8 (12), http://dx.doi.org/10.3390/jmse8120985, URL: https://www.mdpi.com/2077-1312/8/12/985.

Hadadpour, S., Paul, M., Oumeraci, H., 2019. Numerical investigation of wave attenuation by rigid vegetation based on a porous media approach. J. Coast. Res. 92, 92. http://dx.doi.org/10.2112/SI92-011.1.

Hemminga, M.A., Duarte, C.M., 2000. Seagrass Ecology. Cambridge University Press, http://dx.doi.org/10.1017/CBO9780511525551.

Hu, Z., Suzuki, T., Zitman, T., Uittewaal, W., Stive, M., 2014. Laboratory study on wave dissipation by vegetation in combined current–wave flow. Coast. Eng. 88, 131–142. http://dx.doi.org/10.1016/j.coastaleng.2014.02.009, URL: https://www.sciencedirect.com/science/article/pii/S0378383914000416.

Keulegan, G., Carpenter, L., 1958. Forces on cylinders and plates in an oscillating fluid. J. Res. Natl. Bur. Stand. 60, 423–440.

Khayyer, A., Gotoh, H., Falahaty, H., Shimizu, Y., 2018. An enhanced ISPH–SPH coupled method for simulation of incompressible fluid–elastic structure interactions. Comput. Phys. Comm. 232, 139–164. http://dx.doi.org/10.1016/j.cpc.2018.05.012.

Khayyer, A., Shimizu, Y., Gotoh, H., Nagashima, K., 2021. A coupled incompressible SPH-Hamiltonian SPH solver for hydroelastic FSI corresponding to composite structures. Appl. Math. Model. 94, 242–271. http://dx.doi.org/10.1016/j.apm.2021.01.011.

Kobayashi, N., 1993. Wave attenuation by vegetation. J. Waterw. Port Coast. Ocean Eng. 119, 30–48.

Koch, E.W., Sanford, L.P., Chen, S.-N., Shafer, D.J., Smith, J.M., 2006. Waves in Seagrass Systems: Review and Technical Recommendations. System-Wide Water Resources Research Program and Submerged Aquatic Vegetation Restoration Research Program, p. 90.

Kutija, V., Hong, H.T.M., 1996. A numerical model for assessing the additional resistance to flow introduced by flexible vegetation. J. Hydraul. Res. 34 (1), 99–114. http://dx.doi.org/10.1080/00221689609498766, arXiv:https://doi.org/10.1080/00221689609498766.

Lo, E.Y.M., Shao, S., 2002. Simulation of near-shore solitary wave mechanics by an incompressible SPH method. Appl. Ocean Res. 24 (5), 275–286. http://dx.doi.org/10.1016/S0141-1187(03)00002-6, URL: https://www.sciencedirect.com/science/article/pii/S0141118703000026.

Luhar, M., Coutu, S., Infantes, E., Fox, S., Nepf, H., 2010. Wave-induced velocities inside a model seagrass bed. J. Geophys. Res.: Oceans 115, http://dx.doi.org/10.1029/2010JC006345.

Luhar, M., Infantes, E., Orfila, A., Terrados, J., Nepf, H.M., 2013. Field observations of wave-induced streaming through a submerged seagrass (Posidonia oceanica) meadow. J. Geophys. Res.: Oceans 118, 1955–1968. http://dx.doi.org/10.1002/jgrc.20162.

Luhar, M., Nepf, H.M., 2016. Wave-induced dynamics of flexible blades. J. Fluids Struct. 61, 20–41. http://dx.doi.org/10.1016/j.jfluidstructs.2015.11.007.

Marjoribanks, T.I., Hardy, R.J., Lane, S.N., Parsons, D.R., 2014. High-resolution numerical modelling of flow—vegetation interactions. J. Hydraul. Res. 52 (6), 775–793. http://dx.doi.org/10.1080/00221686.2014.948502, arXiv:https://doi.org/10.1080/00221686.2014.948502.

Marjoribanks, T.I., Paul, M., 2022. Modelling flow-induced reconfiguration of variable rigidity aquatic vegetation. J. Hydraul. Res. 60 (1), 46–61. http://dx.doi.org/10.1080/00221686.2020.1866693, arXiv:https://doi.org/10.1080/00221686.2020.1866693.

Martínez-Estévez, I., Domínguez, J., Tagliafierro, B., Canelas, R., García-Feal, O., Crespo, A., Gómez-Gesteira, M., 2023a. Coupling of an SPH-based solver with a multiphysics library. Comput. Phys. Comm. 283, 108581. http://dx.doi.org/10.1016/j.cpc.2022.108581, URL: https://www.sciencedirect.com/science/article/pii/S0010465522003009.

Martínez-Estévez, I., Tagliafierro, B., Rahi, J.E., Domínguez, J., Crespo, A., Troch, P., Gómez-Gesteira, M., 2023b. Coupling an SPH-based solver with an FEA structural solver to simulate free surface flows interacting with flexible structures. Comput. Methods Appl. Mech. Engrg. 410, 115989. http://dx.doi.org/10.1016/j.cma.2023.115989, URL: https://www.sciencedirect.com/science/article/pii/S0045782523001123.

Mattis, S.A., Kees, C.E., Wei, M.V., Dimakopoulos, A., Dawson, C.N., 2019. Computational model for wave attenuation by flexible vegetation. J. Waterw. Port Coast. Ocean Eng. 145, http://dx.doi.org/10.1061/(asce)ww.1943-5460.0000487.

Mendez, F., Losada, I., 2004. An empirical model to estimate the propagation of random breaking and nonbreaking waves over vegetation fields. Coast. Eng. 51, 103–118. http://dx.doi.org/10.1016/j.coastaleng.2003.11.003.

Mendez, F.J., Losada, I.J., Losada, M.A., 1999. Hydrodynamics induced by wind waves in a vegetation field. 104.

Monaghan, J., 1992. Smoothed particle hydrodynamics. Annu. Rev. Astron. Astrophys. http://dx.doi.org/10.1887/0750304588/b485b3.

Monaghan, J., 1994. Simulating free surface flows with SPH. J. Comput. Phys. 110 (2), 399–406. http://dx.doi.org/10.1006/jcph.1994.1034, URL: https://www.sciencedirect.com/science/article/pii/S0021999184710345.

Morison, J., Johnson, J., Schaaf, S., 1950. The force exerted by surface waves on piles. J. Pet. Technol. 2 (05), 149–154. http://dx.doi.org/10.2118/950149-G.

Mullarney, J.C., Henderson, S.M., 2010. Wave-forced motion of submerged single-stem vegetation. J. Geophys. Res.: Oceans 115 (C12), http://dx.doi.org/10.1029/2010JC006448, URL: https://agupubs.onlinelibrary.wiley.com/doi/abs/10.1029/2010JC006448.

Narayan, S., Beck, M.W., Reguero, B.G., Losada, I.J., Wesenbeeck, B.V., Pontee, N., Sanchirico, J.N., Ingram, J.C., Lange, G.M., Burks-Copes, K.A., 2016. The effectiveness, costs and coastal protection benefits of natural and nature-based defences. PLoS ONE 11, http://dx.doi.org/10.1371/journal.pone.0154735.

Nepf, H.M., 1999. Drag, turbulence, and diffusion in flow through emergent vegetation. Water Resour. Res. 35, 479–489. http://dx.doi.org/10.1029/1998WR900069.

O'Connor, J., Rogers, B.D., 2021. A fluid–structure interaction model for free-surface flows and flexible structures using smoothed particle hydrodynamics on a GPU. J. Fluids Struct. 104, http://dx.doi.org/10.1016/j.jfluidstructs.2021.103312.

Ondiviela, B., Losada, I.J., Lara, J.L., Maza, M., Galván, C., Bouma, T.J., van Belzen, J., 2014. The role of seagrasses in coastal protection in a changing climate. Coast. Eng. 87, 158–168. http://dx.doi.org/10.1016/j.coastaleng.2013.11.005, URL: https://www.sciencedirect.com/science/article/pii/S0378383913001889. Coasts@Risks: THESEUS, a new wave in coastal protection.

Paquier, A.E., Oudart, T., Bouteiller, C.L., Meulé, S., Larroudé, P., Dalrymple, R.A., 2021. 3D numerical simulation of seagrass movement under waves and currents with GPUSPH. Int. J. Sediment Res. 36, 711–722. http://dx.doi.org/10.1016/j.ijsrc.2020.08.003.

Paul, M., Amos, C.L., 2011. Spatial and seasonal variation in wave attenuation over Zostera noltii. J. Geophys. Res.: Oceans 116, http://dx.doi.org/10.1029/2010JC006797.

Ralph, P., Durako, M., Enríquez, S., Collier, C., Doblin, M., 2007. Impact of light limitation on seagrasses. J. Exp. Mar. Biol. Ecol. 350 (1), 176–193. http://dx.doi.org/10.1016/j.jembe.2007.06.017, URL: https://www.sciencedirect.com/science/article/pii/S0022098107003152. The Biology and Ecology of Seagrasses.

Rankin, C., Nour-Omid, B., 1988. The use of projectors to improve finite element performance. Comput. Struct. 30 (1), 257–267. http://dx.doi.org/10.1016/0045-7949(88)90231-3, URL: https://www.sciencedirect.com/science/article/pii/0045794988902313.

Reidenbach, M.A., Thomas, E.L., 2018. Influence of the Seagrass, Zostera marina, on wave attenuation and bed shear stress within a shallow coastal bay. Front. Mar. Sci. 5, http://dx.doi.org/10.3389/fmars.2018.00397.

Sarpkaya, T., O'Keefe, J.L., 1996. Oscillating flow about two and three-dimensional bilge keels. J. Offshore Mech. Arct. Eng. 118 (1), 1–6. http://dx.doi.org/10.1115/1.2828796.

Smagorinsky, J., 1963. General circulation experiments with the primitive equations: I. The basic experiment. Mon. Weather Rev. 91 (3), 99–164. http://dx.doi.org/10.1175/1520-0493(1963)091<0099:GCEWTP>2.3.CO;2, URL: https://journals.ametsoc.org/view/journals/mwre/91/3/1520-0493_1963_091_0099_gcewtp_2_3_co_2.xml.

Stratigaki, V., Manca, E., Prinos, P., Losada, I.J., Lara, J.L., Sclavo, M., Amos, C.L., Cáceres, I., Sánchez-Arcilla, A., 2011. Large-scale experiments on wave propagation over Posidonia oceanica. J. Hydraul. Res. 49, 31–43. http://dx.doi.org/10.1080/00221686.2011.583388.

Suzuki, T., García-Feal, O., Domínguez, J.M., Altomare, C., 2022. Simulation of 3D overtopping flow–object–structure interaction with a calibration-based wave generation method with DualSPHysics and SWASH. Comput. Part. Mech. 9, 1003–1015. http://dx.doi.org/10.1007/s40571-022-00468-8.

Suzuki, T., Hu, Z., Kumada, K., Phan, L.K., Zijlema, M., 2019. Non-hydrostatic modeling of drag, inertia and porous effects in wave propagation over dense vegetation fields. Coast. Eng. 149, 49–64. http://dx.doi.org/10.1016/j.coastaleng.2019.03.011.

Tasora, A., Serban, R., Mazhar, H., Pazouki, A., Melanz, D., Fleischman, J., Taylor, M., Sugiyama, H., Negrut, D., 2016. Chrono: An open source multi-physics dynamics engine. In: Lecture Notes in Computer Science (Including Subseries Lecture Notes in Artificial Intelligence and Lecture Notes in Bioinformatics), Vol. 9611. pp. 19–49. http://dx.doi.org/10.1007/978-3-319-40361-8_2.

Vacondio, R., Altomare, C., De Leffe, M., et al., 2021. Grand challenges for Smoothed Particle Hydrodynamics numerical schemes. Comput. Part. Mech. 8, 575–588. http://dx.doi.org/10.1007/s40571-020-00354-1.

van Veelen, T.J., Fairchild, T.P., Reeve, D.E., Karunarathna, H., 2020. Experimental study on vegetation flexibility as control parameter for wave damping and velocity structure. Coast. Eng. 157, 103648. http://dx.doi.org/10.1016/j.coastaleng.2020.103648, URL: https://www.sciencedirect.com/science/article/pii/S0378383919300663.

Vuik, V., Jonkman, S.N., Borsje, B.W., Suzuki, T., 2016. Nature-based flood protection: The efficiency of vegetated foreshores for reducing wave loads on coastal dikes. Coast. Eng. 116, 42–56. http://dx.doi.org/10.1016/j.coastaleng.2016.06.001, URL: https://www.sciencedirect.com/science/article/pii/S0378383916301004.

Wendland, H., 1995. Piecewise polynomial, positive definite and compactly supported radial functions of minimal degree. Adv. Comput. Math. 4, 389–396.

Yang, Q., Jones, V., McCue, L., 2012. Free-surface flow interactions with deformable structures using an SPH-FEM model. Ocean Eng. 55, 136–147. http://dx.doi.org/10.1016/j.oceaneng.2012.06.031.

Yin, K., Xu, S., Huang, W., Liu, S., Li, M., 2021. Numerical investigation of wave attenuation by coupled flexible vegetation dynamic model and XBeach wave model. Ocean Eng. 235, http://dx.doi.org/10.1016/j.oceaneng.2021.109357.

Zeller, R.B., Weitzman, J.S., Abbett, M.E., Zarama, F.J., Fringer, O.B., Koseff, J.R., 2014. Improved parameterization of seagrass blade dynamics and wave attenuation based on numerical and laboratory experiments. Limnol. Oceanogr. 59, 251–266. http://dx.doi.org/10.4319/lo.2014.59.1.0251.

Zhang, F., Crespo, A., Altomare, C., et al., 2018. DualSPHysics: A numerical tool to simulate real breakwaters. J. Hydrodyn. 30 (1), 95–105. http://dx.doi.org/10.1007/s42241-018-0010-0.

Zhu, L., Zou, Q.-P., Huguenard, K., Fredriksson, D.W., 2020. Mechanisms for the asymmetric motion of submerged aquatic vegetation in waves: A consistent-mass cable model. J. Geophys. Res.: Oceans 125 (2), e2019JC015517. http://dx.doi.org/10.1029/2019JC015517, URL: https://agupubs.onlinelibrary.wiley.com/doi/abs/10.1029/2019JC015517, arXiv:https://agupubs.onlinelibrary.wiley.com/doi/pdf/10.1029/2019JC015517. e2019JC015517 10.1029/2019JC015517.

Zijlema, M., Stelling, G., Smit, P., 2011. SWASH: An operational public domain code for simulating wave fields and rapidly varied flows in coastal waters. Coast. Eng. 58 (10), 992–1012. http://dx.doi.org/10.1016/j.coastaleng.2011.05.015, URL: https://www.sciencedirect.com/science/article/pii/S0378383911000974.

Zinke, P., 2012. Application of a porous media approach for vegetation flow resistance. In: River Flow 2012 - Proceedings of the International Conference on Fluvial Hydraulics, Vol. 1. pp. 301–308.